UNCERTAINTY PROPAGATION IN NEURONAL DYNAMICAL SYSTEMS

ALDEMAR TORRES VALDERRAMA [•,⋆], JOKE BLOM [⋆]

Abstract. One of the most notorious characteristics of neuronal electrical activity is its variability, whose origin is not just instrumentation noise, but mainly the intrinsically stochastic nature of neural computations. Neuronal models based on deterministic differential equations cannot account for such variability, but they can be extended to do so by incorporating random components. However, the computational cost of this strategy and the storage requirements grow exponentially with the number of stochastic parameters, quickly exceeding the capacities of current supercomputers. This issue is critical in Neurodynamics, where mechanistic interpretation of large, complex, nonlinear systems is essential. In this paper we present accurate and computationally efficient methods to introduce and analyse variability in neurodynamic models depending on multiple uncertain parameters. Their use is illustrated with relevant examples.

Keywords. Neurodynamics ⋆ Uncertainty Quantification ⋆ Sparse grid quadrature ⋆ Hodgkin-Huxley model ⋆ Neuronal Noise.

⋆ CWI, Amsterdam, the Netherlands
• Department of Neurology and Neurosurgery University, Medical Center Utrecht, the Netherlands
E-mail: atorresv[at]cwi.nl, joke.blom[at]cwi.nl

1. Introduction

Variability is a trademark of realistic neuronal systems, for instance, synaptic inputs can elicit responses in one cell but not in another, and neurons can have different responses to the same inputs or identical responses to distinct inputs ([26]). Experimental and computational evidence suggest that such variability is not a nuisance, but that it might be an integral component of brain computations ([14, 11, 35, 10, 21]). For instance, noise in synaptic inputs to individual neurons can facilitate detection of signals that are small compared with the classical detection threshold, enhancing the cells responsiveness and refining their temporal processing abilities ([12]). In neural networks, variability among individual cells and in their coupling parameters influences their collective response to an external signal, as well as their synchronisation properties ([37, 30, 29, 49, 19]).

Biophysical models of neural electrical activity based on systems of Ordinary Differential Equations (ODE) can provide useful insights into the dynamics of neuronal systems and signal transmission in neural tissue, however in their deterministic form they cannot account for neuronal variability. A common strategy to overcome this limitation, is to introduce stochastic components in the models. Such stochastic components account for voltage fluctuations that we don't care to study in detail, or from external influences that cannot be predicted. For example, in the Point-Conductance model ([39, 31]), fluctuations in synaptic activity are represented by fast glutamatergic and GABAergic conductances described by a random-walk processes. This allows to estimate the response of a neuron to stochastic synaptic input and reproduce in vivo-like activity. Although such stochastic approaches have proved useful in interpreting electrophysiological data, ([12]), introducing random

elements in deterministic models becomes a challenging computational problem as the number of uncertain parameters increases: the computational cost of tensor products rises exponentially with the number of random parameters, and rapidly surpasses the storage and processing capacities of even the most powerful current supercomputers.

The purpose of this paper is to introduce methods to incorporate and analyse the propagation of probabilistic uncertainty in dynamic models with a moderate number of random parameters. This problem is common in Neuroscience, where the subject of study are complex dynamical systems with multiple nonlinear elements ([26, 13, 8, 47]). Indeed, dynamic models of neural systems are generally cast in the form of intricate nonlinear ODE systems, which typically comprise multiple parameters that must be determined experimentally. In practice it is common to use such ODE models with their parameters fixed to certain numerical values. However, these numbers can often be estimated only after hundreds of repeated electrophysiological measurements, and should therefore be regarded as potential sources of probabilistic uncertainty, since due to nonlinearity, even their small fluctuation can yield important changes in the model output. This is particularly crucial for neuronal models, which are archetypical nonlinear dynamical systems ([42]). These considerations suggest that in order to provide valid mechanistic interpretations of neural circuits in the brain, and to facilitate principled interpretations of data from experiments in vitro and in vivo, biophysical models of neuronal systems should incorporate uncertainty as a defining feature, since its effects cannot be captured by e.g., increasing the resolution of the classical numerical algorithms, if stochasticity is not an intrinsic part of the models.

Another important feature of nonlinear dynamical systems with multiple components, is that some of them might exhibit little influence on the model response, whereas others might account for most of the model's output variability. Identifying a priori parameters that are decisive for the model response is crucial for experimental design, since influential parameters may require additional measurements or refined experimental techniques ([33, 3, 2]) . By incorporating uncertainty, the predictive power of dynamic models can be exploited for the preparation and planning of (electrophysiological) measurements. However, in models with several stochastic parameters, that is, with multiple sources of uncertainty, it is generally not obvious where does the variability in the model output come from, based solely on inspection of the ODEs. In this paper we introduce non-intrusive, accurate and computationally efficient methods to undertake such analyses in complex nonlinear dynamical systems.

In Sec. 2, propagation of uncertainty will be framed in a probabilistic context, where uncertainty is parametrized by a set of random variables. We shall see that the quantification of variability in the model output and the analysis of parameter sensitivity can be reduced to multidimensional quadratures, and introduce accurate and efficient methods for their computation using nested numerical integration formulas defined on sparse grids ([6, 16]) based on Smolyak's algorithm ([43]). In Sec. 3 we apply the method to investigate propagation of probabilistic uncertainty in models of individual neurons with linear and nonlinear dependence on uncertain parameters. In the linear case, a simple analytic solution is presented, the nonlinear cases will be approached numerically. In particular, we investigate uncertainty propagation through the action potential mechanism in the classical Hodgkin-Huxley (HH) model ([22]), a non-trivial example regarded as "the most important model in all physiological literature" ([27]). This model depends on eleven potentially uncertain parameters, and exhibits strong nonlinear dynamics. We demonstrate how uncertainty in the model

output can be efficiently computed, and investigate its consequences for neurocomputational properties. The parameters that contribute the most to neuronal variability are identified, which for the HH model have a direct biophysical interpretation. Some methodological remarks and further comments on the examples are presented in Sec. 4, followed by conclusions in Sec. 5. We stress that although the examples focus on the dynamics of individual neurons, the methods presented in this paper are directly applicable to neural networks consisting of a moderate number of cells.

2. Methods

This section describes computationally efficient methods to incorporate uncertainty in deterministic nonlinear ODE systems. First, the problem of uncertainty propagation is formulated in a probabilistic context, showing how it can be reduced to quadratures of functions of the response surface associated with a dynamic model. Next, efficient methods are presented to compute such integrals with nested quadratures defined on sparse grids using Smolyak's construction. Relevant examples are presented in the subsequent section.

2.1. Problem formulation.

We consider neurodynamic models formulated as systems of ordinary nonlinear differential equations of the form

$$\dot{\mathbf{x}}(t,\boldsymbol{\lambda}) = \mathbf{F}(\mathbf{x}(t,\boldsymbol{\lambda})), \tag{1}$$

with $\mathbf{x}(t,\boldsymbol{\lambda}) = [x_1(t,\boldsymbol{\lambda}),\ldots,x_n(t,\boldsymbol{\lambda})]^T : R \times R^d \to R \times R^n$ where $\boldsymbol{\lambda} = [\lambda_{\mathbf{1}},\ldots,\lambda_d] \in R^d$ is a vector of d real parameters, and $t \in R$ represents time. An example to be discussed in Sec. 3 is the Hodgkin-Huxley model ([22])

$$\mathbf{F}(\mathbf{x}(t,\boldsymbol{\lambda})) = \begin{bmatrix} -\frac{\overline{g}_{Na}}{C} m^3 h (v - E_{Na}) - \frac{\overline{g}_K}{C} n^4 (v - E_K) - \frac{\overline{g}_L}{C}(v - E_L) + I \\ (1-n)k_{1n} - nk_{-1n} \\ (1-m)k_{1m} - mk_{-1m} \\ (1-h)k_{1h} - hk_{-1h} \end{bmatrix}, \tag{2}$$

where $\mathbf{x}(t,\boldsymbol{\lambda}) = [v(t,\boldsymbol{\lambda}), m(t,\boldsymbol{\lambda}), n(t,\boldsymbol{\lambda}), h(t,\boldsymbol{\lambda})]^T$. $v(t,\boldsymbol{\lambda})$ is the electrical potential across a neuron membrane, $m(t,\boldsymbol{\lambda}), h(t,\boldsymbol{\lambda})$ are gating variables associated with the activation and inactivation of Na^+ ion currents respectively, and $n(t,\boldsymbol{\lambda})$ is a gating variable associated with the activation of K^+ ions current. The model includes a vector $\boldsymbol{\lambda}$ of eleven parameters

$$\boldsymbol{\lambda} = [v_0, m_0, n_0, h_0, \overline{g}_{Na}, \overline{g}_K, \overline{g}_L, E_{Na}, E_K, E_L, C], \tag{3}$$

namely, four intial conditions v_0, m_0, n_0, h_0, three parameters describing the maximum conductances $\overline{g}_{Na}, \overline{g}_K, \overline{g}_L$, corresponding to Na^+, K^+ and leakage ion currents respectively, three parameters describing their equilibrium Nernst potentials E_{Na}, E_K, E_L, and the membrane capacitance C. In computational models it is common practice to treat $\boldsymbol{\lambda}$ as a set of scalar constants. However, these values must be obtained experimentally and are in principle uncertain.

To incorporate and analyse the effects of such uncertainty into dynamic models of the type described by Eq. (1), let us consider the probability space $(\boldsymbol{\Theta}, F, P)$, with $\boldsymbol{\Theta}$ the set of events containing all possible outcomes of an (electrophysiological) experiment, F a $\sigma-$algebra of events and P a probability measure. With $\boldsymbol{\theta} \in \boldsymbol{\Theta}$ representing an elementary event, the stochastic counterpart of Eq. (1) can be formulated as

$$\dot{\mathbf{x}}(t,\boldsymbol{\theta}) = \mathbf{F}(x(t,\boldsymbol{\theta})) \quad \mathbf{x} \in T \times \boldsymbol{\Theta}, \tag{4}$$

where T represents the time interval during which measurements are performed. The probabilistic uncertainty introduced by the random parameters $\boldsymbol{\theta}$, propagates through the model according to its intrinsic (possibly nonlinear) dynamics, therefore, $\mathbf{x}(t, \boldsymbol{\theta})$ is no longer deterministic and must be described probabilistically.

To compute the propagation of probabilistic uncertainty numerically, the infinite dimensional probability space $(\boldsymbol{\Theta}, F, P)$, must be reduced to a finite dimensional space. This can be performed by parametrizing the random events $\boldsymbol{\theta}$ in terms of a set of independent random variables $\boldsymbol{\xi} = \{\xi_i\}_{i=1}^d$. The probability distributions associated with these random variables, denoted by $\rho_i(\xi_i)$, describe our knowledge about the uncertainty in the parameters $\boldsymbol{\lambda}$. Under the independence assumption, the joint probability density function of $\boldsymbol{\xi}$ is

$$\rho(\xi_1, \ldots, \xi_d) = \prod_{i=1}^{d} \rho_i(\xi_i), \quad \boldsymbol{\xi} \in \Gamma, \tag{5}$$

with $\Gamma = \prod_{i=1}^d \Gamma_i$, where $\Gamma_i = \xi_i(\boldsymbol{\Theta})$ are the images of ξ_i. With this parameterization of the probability space, Eq. (4) contains all the information necessary to characterize the model's output: *each instant in time has associated a probability distribution characterising its uncertainty,* a conceptual representation of this is shown in Fig. 1.

2.2. **Uncertainty quantification reduced to quadratures.** The probability distribution associated with $\mathbf{x}(t, \boldsymbol{\xi})$ contains all the information necessary for uncertainty quantification. A less fundamental but adequate practical characterisation of output variability can be obtained in terms of its moments. This characterisation leads to a quadrature problem in terms of the response surface $\mathbf{x}(t, \boldsymbol{\xi}) \in T \times \Gamma$. At each instant in time $t \in T$, the expected value of the model output can be obtained as

$$E\left[\mathbf{x}(t, \boldsymbol{\xi})\right] = \int \ldots \int \mathbf{x}(t, \xi_1, \ldots, \xi_d) \prod_{i=1}^{d} \rho_i(\xi_i) d\xi_i, \tag{6}$$

with $\mathbf{x}(t, \xi_1, \ldots, \xi_d)$ the solution of the discretized system Eq. (4). Likewise, the variance of the model output can be obtained as

$$\begin{aligned} V\left[\mathbf{x}(t, \boldsymbol{\xi})\right] &= \int \ldots \int \left(\mathbf{x}(t, \xi_1, \ldots, \xi_d) - E\left[\mathbf{x}(t, \boldsymbol{\xi})\right]\right)^2 \prod_{i=1}^{d} \rho_i(\xi_i) d\xi_i \\ &= \int \ldots \int \mathbf{x}^2(t, \xi_1, \ldots, \xi_d) \prod_{i=1}^{d} \rho_i(\xi_i) d\xi_i - E^2\left[\mathbf{x}(t, \boldsymbol{\xi})\right]. \end{aligned} \tag{7}$$

For model interpretation and experimental design, we must also consider the conditional expectation, which accounts for the expected dynamic outcome when the stochastic parameter ξ_j is fixed to a particular value $\tilde{\xi}_j$ and is therefore no longer a source of uncertainty in the model. The conditional expectation can be expressed as

$$E\left[\mathbf{x}(t, \boldsymbol{\xi}) | \xi_j = \tilde{\xi}_j\right] = \int \ldots \int \mathbf{x}(t, \xi_1, \ldots, \tilde{\xi}_j, \ldots, \xi_d) \prod_{\substack{i=1 \\ i \neq j}}^{d} \rho_i(\xi_i) d\xi_i. \tag{8}$$

The corresponding conditional variance provides complementary information about the importance of the contribution of a random parameter to the uncertainty of the model's output variance and

can be expressed in the form

$$V\left[\mathbf{x}(t,\boldsymbol{\xi})|\xi_j=\tilde{\xi}_j\right]=\int\dots\int\mathbf{x}^2(t,\xi_1,\dots,\tilde{\xi}_j,\dots,\xi_d)\prod_{\substack{i=1\\i\neq j}}^{d}\rho_i(\xi_i)d\xi_i-E^2\left[\mathbf{x}(t,\boldsymbol{\xi})|\xi_j=\tilde{\xi}_j\right]. \tag{9}$$

A related dimensionless quantity that allows to compare the relative effect of the different sources of uncertainty in the model can be obtained by noting that the expected value of the conditional variance $E\left[V\left[\mathbf{x}(t,\boldsymbol{\xi})|\xi_j=\tilde{\xi}_j\right]\right]$ equals

$$\int\dots\int\mathbf{x}^2(t,\xi_1,\dots,\xi_j,\dots,\xi_d)\prod_{i=1}^{d}\rho_i(\xi_i)d\xi_i-\int\dots\int E^2\left[\mathbf{x}(t,\boldsymbol{\xi})|\xi_j=\tilde{\xi}_j\right]\rho_j(\tilde{\xi}_j)d\tilde{\xi}_j.$$

Subtracting the previous equation from the total variance, (Eq. (7)) one obtains

$$V\left[\mathbf{x}(t,\boldsymbol{\xi})\right]-E\left[V\left[\mathbf{x}(t,\boldsymbol{\xi})|\xi_j=\tilde{\xi}_j\right]\right]=K_j-E^2\left[\mathbf{x}(t,\boldsymbol{\xi})\right] \tag{10}$$

where

$$\begin{aligned}
K_j &= \int\dots\int E^2\left[\mathbf{x}(t,\boldsymbol{\xi})|\xi_j=\tilde{\xi}_j\right]\rho_j(\tilde{\xi}_j)d\tilde{\xi}_j\\
&= \int\dots\int\left\{\int\dots\int\mathbf{x}(t,\xi_1,\dots,\tilde{\xi}_j,\dots,\xi_d)\prod_{\substack{i=1\\i\neq j}}^{d}\rho_i(\xi_i)d\xi_i\right\}^2\rho_j(\tilde{\xi}_j)d\tilde{\xi}_j\\
&= \int\dots\int\left\{\int\dots\int\mathbf{x}(t,\xi_1,\dots,\tilde{\xi}_j,\dots,\xi_d)\mathbf{x}(t,\xi'_1,\dots,\tilde{\xi}_j,\dots,\xi'_d)\prod_{\substack{i=1\\i\neq j}}^{d}\rho_i(\xi_i)d\xi_i\prod_{\substack{i=1\\i\neq j}}^{d}\rho_i(\xi'_i)d\xi'_i\right\}\rho_j(\tilde{\xi}_j)d\tilde{\xi}_j\\
&\Rightarrow \int\dots\int\left[\mathbf{x}(t,\xi_1,\dots,\xi_j,\dots,\xi_d)\mathbf{x}(t,\xi'_1,\dots,\xi_j,\dots,\xi'_d)\right]\prod_{i=1}^{d}\rho_i(\xi_i)d\xi_i\prod_{\substack{i=1\\i\neq j}}^{d}\rho_i(\xi'_i)d\xi'_i. \qquad (11)
\end{aligned}$$

The quantity in square brackets in (11) is a function of the response surface depending on $2d-1$ variables. In this fashion, each stochastic parameter has associated a quadrature in $2d-1$ space of the form (11), whose magnitude indicates the importance of parameter j with respect to the total variability of the model output at each time point.

Expressing (10) in terms of the total variance one obtains the desired dimensionless quantity, which for each instant of time corresponds to the first order sensitivity index from ANOVA theory ([24, 25, 44, 41]), namely

$$S_j(t)=\frac{V\left[\mathbf{x}(t,\boldsymbol{\xi})\right]-E\left[V\left[\mathbf{x}(t,\boldsymbol{\xi})|\xi_j=\tilde{\xi}_j\right]\right]}{V\left[\mathbf{x}(t,\boldsymbol{\xi})\right]}=\frac{K_j-E^2\left[\mathbf{x}(t,\boldsymbol{\xi})\right]}{V\left[\mathbf{x}(t,\boldsymbol{\xi})\right]}. \tag{12}$$

Notice that $S_j(t)\in[0,1]$ with $\sum_{j=1}^{d}S_j(t)\leq 1$ has a direct probabilistic interpretation: a parameter does not contribute to the variance of the model output at instant t if and only if $E\left[V\left[\mathbf{x}(t,\boldsymbol{\xi})|\xi_j=\tilde{\xi}_j\right]\right]=V\left[\mathbf{x}(t,\xi)\right]$ in which case $S_j(t)=0$. On the other hand, the parameter ξ_j is the only source of probabilistic uncertainty if and only if $V\left[\mathbf{x}(t,\boldsymbol{\xi})|\xi_j=\tilde{\xi}_j\right]=0$, which yields $S_j(t)=1$ and $S_j(t)=0$ for $i\neq j$. Numerically, these limiting cases can be obtained more reliably by noting that $E^2\left[\mathbf{x}(t,\boldsymbol{\xi})\right]$ can be cast in the form of Eq. (11), namely

$$\int\dots\int\left[\mathbf{x}(t,\xi_1,\dots,\xi_j,\dots,\xi_d)\mathbf{x}(t,\xi'_1,\dots,\xi'_j,\dots,\xi'_d)\right]\prod_{i=1}^{d}\rho_i(\xi_i)d\xi_i\prod_{j=1}^{d}\rho_j(\xi'_j)d\xi'_j, \tag{13}$$

Although in this form the computation of the mean squared requires integration in $2d$ dimensions instead of $2d-1$, it often leads to more reliable estimates of the sensitivity indices through Eq. (12). By removing the constraint $i \neq j$ in Eq. (11), i.e., by introducing an extra dummy variable which does not appear in the integrand, all variance quadratures can be obtained with the same sparse grid in $2d$ space provided that the pdfs are properly normalised.
In summary, by reducing the uncertainty quantification problem to quadratures in terms of the response surface $\mathbf{x}(t, \xi_1, \ldots, \xi_d)$ associated with the dynamic model, Eqs. (6), (7), (12) and (13), allow not only to estimate the expected value of a model output, but also its variability and where does this uncertainty come from, that is, which parameters of the model contribute the most to the uncertainty in the output. The computational task of evaluating such quadratures will now be addressed.

2.3. **Uncertainty propagation through sparse grid quadrature.** A standard method for approximating the multivariate integral of a function defined in a box-shaped domain, involves computing function values at a set of support nodes, obtained from the tensor product of the individual m univariate nodes ([46, 7]). Such an approach is only feasible in low dimensions, that is, for a small number of random parameters d, since the number of function evaluations increases as m^d , with m the number of nodes in the unidimensional quadrature rule. Neurodynamic models can include dozens of potentially stochastic parameters, in which case a direct computation of the full tensor product exceeds the storage and processing capacities of current supercomputers. More efficient integration methods become therefore indispensable.
A better strategy to the full tensor product of univariate quadratures, is to find a selection of points in the parameter space Γ to achieve a good approximation of moments of the response surface $\mathbf{x}(t, \xi_1, \ldots, \xi_d)$. This can be achieved by constructing a nested sparse grid in the multi-dimensional random domain Γ for each time point based on Smolyak's algorithm as follows ([43, 6, 16, 15, 34, 20]). Let us first consider the case of a single random parameter ξ, that is $d = 1$. For a time point $t_k \in T$ and $\xi \in \Gamma$ consider the response surface $x(t_k, \xi) : T \times \Gamma \to T \times R$, and the sequence of univariate quadrature rules

$$I\left[x(t_k, \xi)\right] = \int_{\Gamma} x(t_k, \xi) d\xi \simeq U^i\left[x(t_k, \xi)\right] \tag{14}$$

with

$$U^i\left[x(t_k, \xi)\right] = \sum_{j=1}^{m_i} w_j^i \cdot x(t_k, \xi_j^i), \tag{15}$$

with nodes ξ_j^i and weights w_j^i, with m_i the total number of nodes at level i. A nested response surface quadrature formula can be written recursively using the telescoping quantity

$$\Delta^i = U^i - U^{i-1} \quad \text{with } U^0 := 0$$

for $i \geq 1$. Integrals of the response function can be approximated adding the difference between the quadrature at level i and that at the previous level of approximation by the infinite telescoping sum

$$I\left[x(t_k, \xi)\right] \simeq \sum_{i \in \mathcal{N}} \Delta^i\left[x(t_k, \xi)\right] \tag{16}$$

For multiple random parameters $x(t_k, \boldsymbol{\xi}) : T \times \Gamma_1 \times \Gamma_2 \ldots \times \Gamma_d \to T \times R$ the $d > 1$ dimensional integral $I[x(t_k, \xi_1, \ldots, \xi_d)]$ at time point t_k can be approximated numerically by the tensor product

of univariate quadrature formulas as

$$(U^{i_1} \otimes \cdots \otimes U^{i_d})\left[x(t_k, \xi_1, \ldots, \xi_d)\right] = \sum_{j_1=1}^{m_{i_1}} \cdots \sum_{j_d=1}^{m_{i_d}} x(t_k, \xi_{j_1}^{i_1}, \ldots, \xi_{j_d}^{i_d}) \prod_{n=1}^{d} w_{j_n}^{i_n}. \tag{17}$$

The sums above collect each possible combination of the univariate quadrature formulae and involves $m_{i_1} \cdots m_{i_d}$ terms. For smooth functions, using an alternative construction due to Smolyak ([43]), the number of terms in the tensor product can be reduced by orders of magnitude without affecting the polynomial degree of the multidimensional quadrature ([6, 16, 15, 34, 20]). Smolyak's algorithm can be formulated as follows. Let $\mathbf{i}$ be a multi-index with $i_j > 0$ and $\|\mathbf{i}\|_1 = \sum_{j=1}^{d} i_j$. From the set of all possible index combinations $\mathbf{i} \in \mathcal{N}^d$ the algorithm selects only those whose norm $\|\mathbf{i}\|_1$ is smaller than a constant $l + d - 1$, where $l \in \mathcal{N}$ denotes the quadrature level

$$I\left[x(t_k, \xi_1, \ldots, \xi_d)\right] \simeq \sum_{\|\mathbf{i}\|_1 \leq l+d-1} \Delta^{\mathbf{i}}\left[x(t_k, \xi_1, \ldots, \xi_d)\right], \tag{18}$$

with

$$\Delta^{\mathbf{i}} = (\Delta^{i_1} \otimes \Delta^{i_2} \otimes \cdots \otimes \Delta^{i_d}) \tag{19}$$

From (18) the d dimensional integral of the response surface at each time point for a given level $l \in \mathcal{N}$ can be approximated. This process is illustrated in Fig. 2 for $d = 2$.

From numerical analysis ([45, 32]) it is well known that equidistant nodes are not recommended for numerical integration due to Runge's phenomenon, which creates oscillation at the edges of the integration interval. Other quadrature rules are therefore preferred for multivariate integration in conjunction with Smolyak's construction. Of particular interest are the Gauss-Patterson (GP) formulas, which can integrate exactly polynomials of order $2n + \bar{n} + 2$ using $2n + 1$ nodes, with $\bar{n} = n$ for odd n and $\bar{n} = n - 1$ otherwise. Gauss-Patterson formulas do not exist for all $n \in \mathcal{N}$, but their construction is known for $n = 1, 3, 7, 15, 63, 127$ which is sufficient to generate sparse grid constructions for moderate and high dimensions ([16, 36]). These sequences are nested by construction and achieve the maximal degree of exactness. The abscissas of univariate Gauss-Patterson formula are the n zeros of the Legendre polynomial $P_n(x)$, plus the $n + 1$ zeros of the Stieltjes polynomial F_{n+1} that are orthogonal to the nth Legendre polynomial.

$$\int_{-1}^{1} P_n(z) F_{n+1}(z) z^j dz = 0 \text{ for } j = 0, 1, \ldots, n. \tag{20}$$

F_{n+1} can be computed and stored for fast sparse grid generation by expanding it in terms of Legendre polynomials and solving the associated linear system. Gauss-Patterson quadrature was employed in all uncertainty quantification analyses presented in this article. The first levels of Smolyak's sparse grid construction using Gauss-Patterson nodes are illustrated in Fig. 2. The values of the estimated quadrature at different levels can be used as stopping criterion in an automated numerical implementation, that increases the number of sparse grid nodes, that is, the number of function evaluations, until the difference between levels gets below a desired tolerance. The number of points required to achieve a certain accuracy in the uncertainty estimates, and therefore the computational cost, depend on the isotropic smoothness of the response surface, as well as on the type of nodes and dimensionality of the problem as discussed in Sec. 4.

To assess the accuracy in the computation of time series $f(t)$ such as the means, variances and sensitivity indices, in what follows the weighted RMS error will be employed, namely

$$E_{RMS}(f) = \sqrt{\frac{1}{N_T}\sum_{k=1}^{N_T}\left(\frac{f(t_k)-f^*(t_k)}{max(1,f^*(t_k))}\right)^2}, \tag{21}$$

with N_T the number of time samples t_k, $f(t_k)$ corresponds to the solution at the current level at each time point, $f^*(t_k)$ represents the exact analytic solution (if available), or the numerical solution computed at the highest sparse grid level used, i.e., the most accurate numerical solution is taken as a reference for error analysis. For smooth integrands, sparse grids can exhibit exponential convergence ([23]), in such cases the true accuracy can be much higher that Eq. (21) would suggest.

3. Results

To illustrate the methodology described in Sec. 2, this section considers three examples. The first two are based on Lapicque's Integrate and Fire neuron ([5]) with an oscillatory input current. This model was introduced in ([18]) to investigate the link between gamma rhythmicity in neuronal firing and the selective transmission of information. In its simplest form, the model considers the dynamics of the membrane potential $v(t)$ described by the ODE

$$\frac{dv}{dt} = -\frac{1}{\tau}(v - v_0) + \mu + B\sin(2\pi\gamma t) \tag{22}$$

where τ_m represents the membrane's time constant (see e.g., [8]), and the last two terms in the right hand side represent an external input current. This current mimics the dynamical effects of synchronous spike volleys at frequency γ projected from visual cortex. A closed expression for the response surface corresponding to (22) was obtained in Appendix 1A of ([18]), and reads

$$\begin{aligned} v(t+t_0) &= (\tau\mu + v_0)\left(1 - e^{-t/\tau}\right) \\ &\quad -B\frac{\tau}{\sqrt{4\pi^2\gamma^2\tau^2+1}}\sin(2\pi\gamma t_0 - \theta)\, e^{-t/\tau} \\ &\quad +B\frac{\tau}{\sqrt{4\pi^2\gamma^2\tau^2+1}}\sin(2\pi\gamma t_0 - \theta + 2\pi\gamma t), \end{aligned} \tag{23}$$

with $\theta = \arctan(2\pi\gamma\tau)$.

3.1. Example 1: linear dependence on stochastic parameters.

Let us first consider the case where the amplitude of the incoming synaptic pulses is negligible ($B \approx 0$), and assume that the initial potential $v(t_0)$ and v_0 are measured with some experimental error ε and δ respectively, say $v(t_0) = (0 \pm \varepsilon)$ and $v_0 = (0 \pm \delta)$, whereas the remaining parameters are constants, for which we adopt the values used in Sec. 3 of ([18]), namely $t_0 = 0$, $\tau = 7$ms and $\gamma = 43$Hz, fixing μ such that $\tau\mu = 1$. With these parameters, the response surface Eq. (23) reduces to

$$v(t) = (\mu\tau + v_0)\left(1 - e^{-t/\tau}\right) + v(t_0)e^{-t/\tau}. \tag{24}$$

To study the propagation of uncertainty due to fluctuations in $v(t_o)$ and v_0 through the model, we first introduce the random variables ξ_1 and ξ_2, which we assume to be independent and uniformly

distributed with probability density functions given by

$$\rho_1(\xi_1) = \begin{cases} \frac{1}{2\varepsilon}, \text{ if } 0-\varepsilon \leq \xi_1 \leq 0+\varepsilon \\ 0, \text{ otherwise} \end{cases} \tag{25}$$

$$\rho_2(\xi_2) = \begin{cases} \frac{1}{2\delta}, \text{ if } 0-\delta \leq \xi_2 \leq 0+\delta \\ 0, \text{ otherwise} \end{cases} \tag{26}$$

From Eqs. (6) and (7) the mean and variance of the model output can be computed exactly, which yields

$$E[v(t)] = 1 - e^{-t/\tau} \tag{27}$$

$$V[v(t)] = \frac{1}{3}e^{-2t/\tau}\left(\varepsilon^2 + (e^{t/\tau}-1)^2\delta^2\right). \tag{28}$$

Notice that the previous quantities are independent of ξ_1 and ξ_2, which have been integrated out. Likewise, the sensitivity indices can be obtained from Eq. (12), which yields

$$S_1(t) = S_{v(0)}(t) = \frac{\varepsilon^2}{\left(\varepsilon^2 + (e^{t/\tau}-1)^2\delta^2\right)} \tag{29}$$

$$S_2(t) = S_{v_0}(t) = \frac{(e^{t/\tau}-1)^2\delta^2}{\left(\varepsilon^2 + (e^{t/\tau}-1)^2\delta^2\right)}. \tag{30}$$

Fig. 3(a) and (b) show the response surface for the sub-threshold dynamics at different instants in time. In this example the response surface is a plane, and all quadratures required for the uncertainty analysis can be obtained exactly. Panels (c) and (d) show the mean of the model output, with error bars extending one standard deviation above and below the mean, and the sensitivity indices S_1 and S_2 respectively.

The sensitivy analysis can be interpreted as follows. At the initial time $S_{v_0}(0) = 0$ and $S_{v(0)}(0) = 1$, therefore, variability in the model output can be attributed solely to uncertainty in the initial membrane potential. The influence of the latter decreases as time marches on, and eventually the uncertainty in the equilibrium potential becomes the only source of variability, corresponding to the asymptotic regime $t \to \infty$, where $S_{v_0}(t) = 1$ and $S_{v(0)}(t) = 0$. Notice that $S_{v_0} + S_{v(0)} = 1$ at each time point, since v_0 and $v(0)$ are the only uncertain variables. The bottom panels in Fig. 3 show the error for all quadratures required for the analysis for different levels of a nested sparse grid generated using the unidimensional Gauss-Patterson rule. The error is measured with respect to the exact solution as the maximum absolute value of the difference between estimates for all time points. Panels (e) and (f) show that the accuracy is orders of magnitude higher than that obtainable by the crude Monte Carlo method using the same number of model evaluations. Increasing the number of model evaluations in this linear example is not only superfluous, but also detrimental in terms of accuracy, since it introduces round-off error.

3.2. **Example 2: nonlinear dependence on stochastic parameters.** In this example we consider the case where the amplitude of the synchronised train of excitatory input at frequency γ, described by the oscillatory forcing function $B\sin(2\pi\gamma t)$ in Eq. (22), is not negligible. In contrast to the previous example, in this instance τ_m and γ are considered uncertain parameters measured with a certain experimental error, whereas $v(0) = 0$ and $v_0 = 0$ are treated as constants. This describes the physical situation where there is uncertainty about the values of the membrane's time constant and the frequency of the incoming synchronous synaptic input. Notice that *in this example the uncertain parameters enter the equations through nonlinear terms*, namely exponentials and sinusoids

arising from the particular solutions of the non-homogeneous problem (cf. Eq. (23)). We focus on the sub-threshold dynamics with $\mu = 1/10.5$ms, and $B = 112\text{s}^{-1}$. In this instance, the response surface is highly nonlinear, exhibiting more and more crests and valleys as time marches on. This poses a much more difficult quadrature problem as compared to the previous linear example. The response surface at different times is shown in the top panels of Fig. 4.

To quantify the variability in the model output due to such uncertainty, we introduce the random variables ξ_1 and ξ_2, which we assume to be independent and uniformly distributed with probability density function given by

$$\rho_i(\xi_i) = \begin{cases} \frac{1}{2\varepsilon\mu_i}, \text{ if } \mu_i - \varepsilon\mu_i \leq \xi_i \leq \mu_i + \varepsilon\mu_i \\ 0, \text{ otherwise.} \end{cases} \tag{31}$$

with $\mu_1 = 7$ms and $\mu_2 = 43$Hz nominal values corresponding to those used in ([18]) and $\varepsilon = 0.2$. The middle panels of Fig. 4 show the model output and the sensitivity indexes obtained by the sparse grid method. Notice that in this example the mean stochastic solution differs from the deterministic solution computed at the nominal values of the parameters τ_m and γ.

Fig. 4 shows that initially uncertainty in the membrane time constant is the main source of variability in the model output, this situation changes in the second half of the time series, where the oscillatory term dominates and becomes the major source of variability, as it can be observed from the error bars in (c). The bottom panels show the error for all statistical quantities required for the uncertainty analysis, measured with respect to level 7, which uses 23297 model evaluations (cf. Fig 2), as the maximum absolute value of the difference between estimates for all time points. Notice that in spite of the extreme nonlinearity of the response surface, the GP quadrature yields errors smaller than about 10^{-8} for its higher levels in all quadratures.

3.3. **Example 3: uncertainty propagation in the Hodgkin-Huxley model.** To illustrate the application of the methods described in Sec. 2 in higher dimensions, this example investigates the Hodgkin-Huxley model of action potentials ([22]) Eqs. (2). Uncertainty in the model is introduced by considering the model parameters in Eq. (3) as stochastic variables with uniform probability distributions

$$\rho_i(\xi_i) = \begin{cases} \frac{1}{2\varepsilon\mu_i}, \text{ if } \mu_i - \varepsilon\mu_i \leq \xi_i \leq \mu_i + \varepsilon\mu_i \\ 0, \text{ otherwise} \end{cases} \tag{32}$$

with μ_i the nominal values of the parameters listed in appendix A, which correspond to measurements in the giant squid axon ([22]) and $\varepsilon = 0.2$. There are eleven random parameters in the model (Eq. (3)), requiring 22-dimensional quadrature for the sensitivity analysis through Eqs. (12) and (13) and 11-dimensional quadrature for the computation of the mean through Eq. (6). Figs. 5 and 6 show the results of such analyses. The RMS error for the mean, variance and sensitivity indices for each of the random parameters in the model are summarised in Table 1. For the mean, f^* in Eq. (21) corresponds to the fourth level of a GP sparse grid which has 18591 points. For the variance and conditional variances, a GP sparse grid in 22 dimensions requiring 17249 model evaluations was used. Note that the error estimates in Table 1 are very conservative at the final level shown in Figs. 5 and 6 and discussed below, they are an approximation of the error at the last but one level.

Fig. 5 shows the stochastic dynamics of the membrane potential and that of the activation of K^+ ions current during neuronal discharge, with error bars extending one standard deviation above and below the mean. The different panels show that probabilistic uncertainty is greatest during neuronal discharge both for the action potential and for the gating variables. The mean of the stochastic

model response differs from the deterministic solution, mainly when the membrane depolarization reaches its acme. Fig. 6 shows the sensitivity analysis, which allows to identify what are the mechanisms causing the values of the membrane potential and K^+ ions current to deviate from purely deterministic behaviour. Dynamic changes in the sensitivity of the model for different stages of the action potential are apparent. The sensitivity indices identify two main sources of uncertainty in the model output, namely, the maximum conductance $\bar{g}_K$ and the Na^+ equilibrium Nernst potential E_{Na}, operating mainly during the up stroke of the spike. Fluctuations in the membrane capacitance seem to influence the repolarization dynamics. A second peak in the sensitivity index associated with E_{Na} points to an important contribution of this variable during the refractory period. $m(t)$ exhibits maximal uncertainty during the upstroke phase of the action potential. The membrane capacitance appears to have some effect during repolarization at about $t = 10ms$. $\bar{g}_K$ has a dominant effect in the inactivation of Na^+ ions current, the dynamics of which is known to be particularly important for repolarization ([26]). Uncertainty analysis of the membrane potential $v(t, \boldsymbol{\lambda})$ revealed large fluctuations during neuronal discharge. For instance, the error bars in Fig. 5 show that a threshold for spike detection, set at say 40mV, can fail to detect some of the action potentials, while according to the deterministic model, such threshold should be always suitable for reliable spike detection.

4. Discussion

4.1. **Remarks related to the examples.** Some application scenarios of the proposed methodology were presented. In particular, propagation of probabilistic uncertainty through action potentials as described by the classical Hodgkin-Huxley was investigated. The voltage dependence of conductances in the model, its strong non-linearity, the number and variety of potentially stochastic parameters, as well as its neurophysiological relevance make this model interesting for uncertainty analysis.

Sensitivity analysis based on Eq. (12) revealed that two parameters, namely the maximal conductance $\bar{g}_K$, and the sodium ions equilibrium potential E_{Na} are the major contributors to the model uncertainty. The remaining parameters have little influence in the uncertainty of the model output. These parameters can therefore be fixed to their nominal values without major consequences for the predictive quality of the model output. This result is important since it shows that in a large scale network simulation, it might not be necessary to treat all parameters in the Hodgkin-Huxley model as uncertain, and that with only two stochastic parameters per cell it is possible to incorporate uncertainty in biophysical models of realistic neuronal systems, greatly reducing the dimensionality of the problem and facilitating simulations of larger neuronal populations. Notice also that the output variability in Fig. 4 is considerably smaller than that in Fig. 5, suggesting a variance reduction effect due to synchronous input.

Fig. 8 provides some examples, where variability in the HH model can have consequences on neurocomputational properties of neurons, namely their firing probability and their refractory period after synaptic input. In Fig. 8 (a) two brief current pulses are applied to a deterministic neuron whose membrane potential is initially in equilibrium at 0mV. The first pulse rises the membrane potential, but is not enough to elicit neuronal discharge. After the membrane repolarizes and stabilizes at 0mV, a second stronger pulse is applied, this time the pulse immediately triggers a spike. The stochastic counterpart of this experiment, where the two main sources of probabilistic uncertainty identified in Fig. 6, namely $\bar{g}_K$ and E_{Na}, are treated as random parameters is presented

in (c). The error bars in the response to the first pulse show considerable uncertainty in the model output. This means that due to neuronal variability, in some cases the first small current pulse can indeed trigger action potentials.
In panels (b) and (d) the stronger current pulse is applied first, immediately eliciting a spike. In the deterministic neuronal model (b) the second small pulse fails to trigger a second discharge when applied shortly after the refractory period. In (d), where uncertainty has been incorporated in the model, large variability in its output indicates that in this instance the second pulse could elicit a second action potential that would not be expected according to the purely deterministic model. These examples show that probabilistic uncertainty propagation can have consequences which directly affect neurocomputational properties of neurons, namely, their response to synaptic inputs and their refractory characteristics. This might have implications for their collective behaviour as well as for the efficiency of the neural codes. Work by the authors toward investigating these phenomena is currently in progress.

4.2. **Methodological remarks.** In this paper computationally efficient methods to incorporate variability in neurodynamic models have been introduced, and applied to dynamic models with linear and nonlinear dependence on uncertain parameters. The problem was formulated as a quadrature problem in multiple dimensions, which was solved using sparse grids. The computational advantages of such a formulation are manifold.
First, the computational cost of the proposed method is mainly determined by the number of model evaluations m. The d-dimensional quadrature rule defined as the full tensor product of univariate quadratures (Eq. (17)) requires m^d function evaluations, where m is the number of grid points in one coordinate direction. This indicates an exponential rise in the number of model evaluations required as the number of stochastic parameters increases. This curse of dimensionality prevents the successful application of full tensor product rules to uncertainty quantification when the number of parameters is roughly larger than eight ([46, 7, 23]). For the sparse grid method at level l and dimension d, the number of model evaluations is

$$m_l^d = \sum_{\|\mathbf{i}\|_1 \leq l+d-1} m_{i_1} \dots m_{i_d}, \tag{33}$$

which is in general orders of magnitude smaller than m^d for high dimensions. The discretizations on sparse grids involve $O(m\dot{(}log(m))^{d-1})$ degrees of freedom only. Which means that *the complexity rate depends on the dimension through a logarithmic factor* [6, 16, 15, 34, 20].
A second advantage of studying neuronal variability through the methods in Sec. 2 is the accuracy of quadrature rules. Quadratures using m nodes can integrate all polynomials up to a certain degree exactly. In this paper we have employed Gauss-Patterson rules, which achieve the maximal polynomial accuracy of all nested rules, namely $3m-2$ using $2m+1$ nodes, which is considerably higher than the degree of other nested rules, for instance the Trapezoidal rule, whose polynomial accuracy is 1, and the Clenshaw-Curtis rule, whose abscissas are the extreme points of Tchebyscheff polynomials of the first kind, whose polynomial accuracy is $m-1$ using m nodes. ([6, 16, 15, 34, 20]). Since the number of required nodes n to achieve exactness increases only polynomially with the dimension for reasonably smooth response surfaces, important global sensitivity measures such as Eq. (12) can be obtained accurately.
Although the examples presented above focus on the dynamics of individual neurons, the methods presented in Sec. 2 are directly applicable to more complex dynamical systems, such as neural

networks. In treating such problems, non-intrusive methods such as those described in Sec. 2 offer opportunities for parallelization, which can greatly reduce the (wall clock) computational time. As an example, Fig. 7 shows a parallel implementation of example 3. The figure illustrates how all quadratures required for uncertainty analysis can be performed simultaneously, for they employ different data, generated through model evaluations at distinct nodes. Therefore, these model evaluations can be performed by different processes (workers). The model outputs can then be collected to obtain the values of the mean, variance and sensitivity indices for all time points. It is important to notice that the workers do not need to share data among them, but only report their results to the master node, so there is no additional cost associated with data transfer among processes. To get an idea of the total time required to e.g., obtain the results in the previous section, we notice that each model evaluation takes about 0.26s using Matlab solver ode23 to obtain the numerical solution of Eq. (2) in a four core 2.7GHz Intel processor. An additional interesting advantage of the sparse grid approach is that due to the recursive implementation of the problem (Eq. (2.3)), and the nested structure of sparse grids, it is not necessary to discard previous results when greater accuracy is required. Therefore, all model evaluations can be stored and used to increase accuracy when moving to the next quadrature level. The quadrature difference between levels can be used as stopping criterion in an automated implementation yielding results up to the floating point accuracy desired by the user.

Some limitations of the methods presented must be pointed out and discussed. First, throughout the derivations of Sec. 2 and all numerical experiments it was assumed that uncertainty could be parameterized by a set of independent random variables. Under some circumstances, model parameters might exhibit correlations, although this is not an essential restriction, those might not be accounted for as efficiently by the methodology presented in this paper. By transforming correlated to uncorrelated distributions through, e.g., Rosenblatt ([40]), Nataf ([9]), and Box-Cox ([4]) transformations, some correlation effects can be incorporated in the models. Second, the accuracy of the method depends more or less strongly on the smoothness of the response surface, which has a favorable impact. For instance, in Tables 2 and 3, summarising the RMS errors obtained when a brief external impulse is applied to the neuron, the error in the sensitivity indices is relatively high. In many cases, adaptive quadrature formulas can circumvent such difficulties that arise with non-smooth integrands ([48, 17, 1]). For small and moderate number of dimensions, the convergence rate of the sparse grid method is much faster than that of the Monte Carlo method. (cf. Figs. 3 and 4). However, the performance of the sparse grid method will eventually degrade with increasing number of dimensions due to the error dependence on dimensionality through a logarithmic term. In contrast, the error of the Monte Carlo methods for approximating integrals is independent of d. Therefore, the latter method is generally recommended for large scale simulations. For neurodynamic systems with a moderate number of stochastic parameters as those discussed in this article, uncertainty quantification through sparse grid quadrature might offer much room for investigation. Efficient algorithms for implementation of sparse grid quadrature can be found in ([38, 23]) and TOMS algorithm 847 ([28]).

5. Conclusion

Neural electrical activity is almost always accompanied by considerable amounts of variability, and model parameters obtained in electrophysiological experiments are generally uncertain. In this paper we introduced non-intrusive, accurate and computationally efficient methods to incorporate

and analyse such uncertainty in neurodynamic models based on ODEs to obtain a probabilistic interpretation of their output. Using these methods, we have shown that probabilistic uncertainty can have consequences for neurocomputational properties of individual neurons. Incorporating such uncertainty in biophysical models of neuronal systems can therefore contribute to our mechanistic understanding of the nervous systems and the behaving brain, by facilitating principled interpretations of electrophysiological data from experiments, as well as optimal experimental design. Analysis of the Hodgkin-Huxley model revealed that only two of the eleven potentially stochastic parameters in the model explain most of its output variability, showing that it is possible to considerably reduce the dimensionality of the stochastic version of the model. This opens possibilities to study uncertainty propagation in larger systems such as neural networks, by considering only two random parameters per cell. Work in this direction by the authors is in progress.

6. Acknowledgements

ATV gratefully acknowledges the financial support of the Exact Sciences division of the Netherlands Organisation for Scientific Research NWO grant number: veni 639.071.905 and Prof. Stan Gielen for useful discussions and suggestions. This work was also supported by European Commission's 7th Framework Program BioPreDyn grant number 289434.

Appendix A. Hodgkin-Huxley model nominal parameters

$$k_{1n} = \frac{0.01(10-v)}{\exp\left[\frac{10-v}{10}\right]-1} \tag{34}$$

$$k_{-1n} = 0.125\exp\left[\frac{-v}{80}\right] \tag{35}$$

$$k_{1m} = \frac{0.1(25-v)}{\exp\left[\frac{25-v}{10}\right]-1} \tag{36}$$

$$k_{-1m} = 4\exp\left[\frac{-v}{18}\right] \tag{37}$$

$$k_{1h} = 0.07\exp\left[\frac{-v}{20}\right] \tag{38}$$

$$k_{-1h} = \frac{1}{\exp\left[\frac{30-v}{10}\right]+1} \tag{39}$$

$$C = 1\mu\mathrm{F/cm}^2 \tag{40}$$

$$\overline{g}_K = 36\mu\mathrm{S/cm}^2 \tag{41}$$

$$\overline{g}_{Na} = 120\mu\mathrm{S/cm}^2 \tag{42}$$

$$\overline{g}_L = 0.3\mu\mathrm{S/cm}^2 \tag{43}$$

$$E_K = -12\mathrm{mV} \tag{44}$$

$$E_{Na} = 115\mathrm{mV} \tag{45}$$

$$E_L = 10.613\mathrm{mV} \tag{46}$$

$$I = 150\mathrm{mA} \tag{47}$$

$$n_0 = 0.0003 \tag{48}$$

$$m_0 = 0.0011 \tag{49}$$

$$h_0 = 0.9998 \tag{50}$$

$$v_0 = -10\mathrm{mV} \tag{51}$$

$$n_0 = 0.297^* \tag{52}$$

$$m_0 = 0.00616^* \tag{53}$$

$$h_0 = 0.12^* \tag{54}$$

$$v_0 = 0.001^* \tag{55}$$

$$* = \text{Initial values used in Fig. 8}$$

References

[1] Nitin Agarwal and N. R. Aluru. A domain adaptive stochastic collocation approach for analysis of mems under uncertainties. *J. Comput. Phys.*, 228(20):7662–7688, November 2009.

[2] S. P. Asprey and S. Macchietto. Statistical tools for optimal dynamic model building. *Computers chem. Engng*, 24(2-7):1261–1267, 2000.

[3] J. R. Banga and E. Balsa-Canto. Parameter estimation and optimal experimental design. *Essays in biochemistry*, 45:195–209, 2008.

[4] G. E. P. Box and D. R. Cox. An Analysis of Transformations. *Journal of the Royal Statistical Society. Series B (Methodological)*, 26(2):211–252, 1964.

[5] Nicolas Brunel and MarkC.W. Rossum. Lapicques 1907 paper: from frogs to integrate-and-fire. *Biological Cybernetics*, 97(5-6):337–339, 2007.

[6] Hans-Joachim Bungartz and Michael Griebel. Sparse grids. *Acta Numerica*, 13:147–269, 4 2004.

[7] P.J. Davis and P. Rabinowitz. *Methods of Numerical Integration*. Computer Science and Applied Mathematics. Acad. Press, 1975.

[8] Peter Dayan and L. F. Abbott. *Theoretical Neuroscience: Computational and Mathematical Modeling of Neural Systems*. The MIT Press, 2005.

[9] A. Der Kiureghian and P.L. Liu. *Structural Reliability Under Incomplete Probability Information*. Report. 1985.

[10] A. Destexhe and D. Paré. Impact of network activity on the integrative properties of neocortical pyramidal neurons in vivo. *Journal of neurophysiology*, 81(4):1531–1547, April 1999.

[11] A Destexhe, M Rudolph, J.-M Fellous, and T.J Sejnowski. Fluctuating synaptic conductances recreate in vivo-like activity in neocortical neurons. *Neuroscience*, 107(1):13 – 24, 2001.

[12] A. Destexhe and M. Rudolph-Lilith. *Neuronal Noise*. Springer Series in Computational Neuroscience. Springer, 2012.

[13] GB Ermentrout and D Terman. *Mathematical Foundations of Neuroscience*, 2010.

[14] J. M. Fellous, M. Rudolph, A. Destexhe, and T. J. Sejnowski. Synaptic background noise controls the input/output characteristics of single cells in an in vitro model of in vivo activity. *Neuroscience*, 122(3):811–829, 2003.

[15] Thomas Gerstner. Sparse Grid Quadrature Methods for Computational Finance, 2007.

[16] Thomas Gerstner and Michael Griebel. Numerical integration using sparse grids. *NUMER. ALGORITHMS*, 18:209–232, 1998.

[17] Thomas Gerstner and Michael Griebel. Dimension-adaptive tensor-product quadrature. *Computing*, 71:2003, 2003.

[18] Stan Gielen, Martin Krupa, and Magteld Zeitler. Gamma oscillations as a mechanism for selective information transmission. *Biological Cybernetics*, 103(2):151–165, 2010.

[19] David Golomb and John Rinzel. Dynamics of globally coupled inhibitory neurons with heterogeneity. *Physical Review E*, 48(6):4810–4814, December 1993.

[20] M. Griebel. *Sparse Grids and Related Approximation Schemes for Higher Dimensional Problems*. Sonderforschungsbereich 611, Singuläre Phänomene und Skalierung in Mathematischen Modellen. SFB 611, 2006.

[21] N. Hô and A. Destexhe. Synaptic background activity enhances the responsiveness of neocortical pyramidal neurons. *J. Neurophysiol.*, 84:1488–1496, 2000.

[22] A. L. Hodgkin and A. F. Huxley. A quantitative description of membrane current and its application to conduction and excitation in nerve. *The Journal of Physiology*, 117(4):500–544, August 1952.

[23] M. Holtz. *Sparse grid quadrature in high dimensions with applications in finance and insurance*. Lecture Notes in Computational Science and Engineering, 77. Springer Berlin Heidelberg, 2011.

[24] Toshimitsu Homma and Andrea Saltelli. Importance measures in global sensitivity analysis of nonlinear models. *Reliability Engineering and System Safety*, 52:1–17, 1996.

[25] T. Ishigami and Toshimitsu Homma. An importance quantification technique in uncertainty analysis for computer models. In *International Symposium on Uncertainity Modelling and Analysis (ISUMA'90)*, Dec. 3–6, University of Maryland, 1990.

[26] Eugene M. Izhikevich. *Dynamical Systems in Neuroscience: The Geometry of Excitability and Bursting (Computational Neuroscience)*. The MIT Press, 1 edition, November 2006.

[27] J.P. Keener and J. Sneyd. *Mathematical Physiology*. Interdisciplinary Applied Mathematics. SPRINGER VERLAG GMBH, 1998.

[28] Andreas Klimke and Barbara Wohlmuth. Algorithm 847: Spinterp: piecewise multilinear hierarchical sparse grid interpolation in matlab. *ACM Trans. Math. Softw.*, 31(4):561–579, December 2005.

[29] Tae-Wook Ko and G.B. Ermentrout. Partially locked states in coupled oscillators due to inhomogeneous coupling. *Phys Rev E Stat Nonlin Soft Matter Phys*, 78(1):016203, 2008.

[30] Carlo Laing, Yu Zou, Ben Smith, and Ioannis Kevrekidis. Managing heterogeneity in the study of neural oscillator dynamics. *The Journal of Mathematical Neuroscience*, 2(1):5, 2012.

[31] Petr Lánský and Jean-Pierre Rospars. Ornstein-uhlenbeck model neuron revisited. *Biological Cybernetics*, 72(5):397–406, 1995.

[32] J.H. Mathews and K.D. Fink. *Numerical methods using MATLAB*. Pearson Prentice Hall, 2004.

[33] V.B. Melas. *Functional Approach to Optimal Experimental Design*. Lecture Notes in Statistics. Springer, 2006.

[34] Erich Novak and Klaus Ritter. High dimensional integration of smooth functions over cubes. *Numerische Mathematik*, 75(1):79–97, 1996.

[35] D. Paré, E. Shink, H. Gaudreau, A. Destexhe, and E. J. Lang. Impact of spontaneous synaptic activity on the resting properties of cat neocortical pyramidal neurons in vivo. *J. Neurophysiol.*, 79:1450–1460, 1998.

[36] T. N. L. Patterson. An algorithm for generating interpolatory quadrature rules of the highest degree of precision with preassigned nodes for general weight functions. *ACM Trans. Math. Softw.*, 15(2):123–136, June 1989.

[37] T Perez, CR Mirasso, R Toral, and JD Gunton. The constructive role of diversity in the global response of coupled neuron systems. *Philos Trans R Soc A, Math Phys Eng Sci*, 368(1933):5619–5632, 2010.

[38] K. Petras. Fast calculation of coefficients in the Smolyak algorithm. *Numerical Algorithms*, 26:93–109, February 2001.

[39] L. M. Ricciardi and L. Sacerdote. The Ornstein-Uhlenbeck process as a model for neuronal activity. *Biol. Cybern.*, 35:1–9, 1979.

[40] Murray Rosenblatt. Remarks on a Multivariate Transformation. *The Annals of Mathematical Statistics*, 23(3):470–472, 1952.

[41] Andrea Saltelli. Making best use of model evaluations to compute sensitivity indices. *Computer Physics Communications*, 145(2):280 – 297, 2002.

[42] S.J. Schiff. *Neural control engineering: the emerging intersection between control theory and neuroscience*. Computational Neuroscience Series. The MIT Press, 2011.

[43] SA Smolyak. Quadrature and interpolation formulas for tensor products of certain classes of functions. *Dokl Akad Nauk SSSR*, 4:240–243, 1963.

[44] Ilya M. Sobol. Sensitivity estimates for nonlinear mathematical models (in Russian). *Mathematical Models*, 2:112–118, 1990.

[45] J. Stoer and R. Bulirsch. *Introduction to Numerical Analysis*. Springer, New York, 3 edition, August 2002.

[46] A. H. Stroud. *Approximate calculation of multiple integrals*. Englewood Chiffs, New Jersey: Prentice-Hall, 1971.

[47] P. Wallisch, M. Lusignan, M. Benayoun, T.I. Baker, A.S. Dickey, and N. Hatsopoulos. *MATLAB for Neuroscientists: An Introduction to Scientific Computing in MATLAB*. Elsevier Science, 2010.

[48] Grzegorz W. Wasilkowski and Henryk Wozniakowski. Weighted tensor product algorithms for linear multivariate problems. *J. Complexity*, 15(3):402–447, 1999.

[49] J.A. White, C.C. Chow, Rit J., C. Soto-Trevino, and N. Kopell. Synchronization and oscillatory dynamics in heterogeneous, mutually inhibited neurons. *Journal of Computational Neuroscience*, 5(1), 1998.

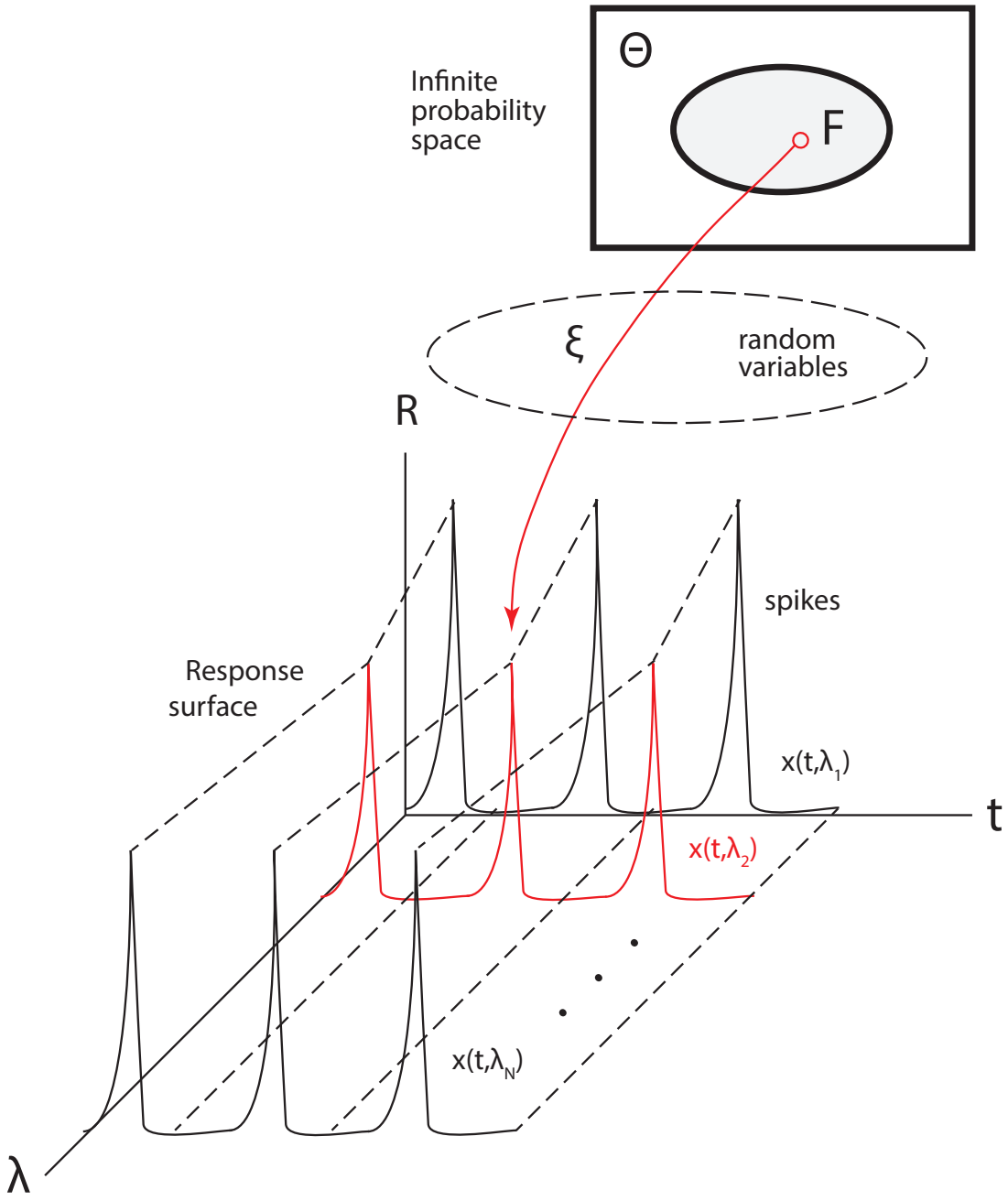

FIGURE 1. Conceptual view of uncertainty propagation in dynamical systems. The model output $x(t, \lambda)$ plotted in the parameter space for all possible values of λ generates the response surface of a random experiment with outcomes F. The outcomes $x(t, \lambda_i)$ are generally different depending on how λ_i affects the system's intrinsic dynamics. To quantify variability in the model output, the infinite probability space can be parametrized by random variables ξ, which assume values according to a given probability rule. Each realization of ξ, represented by the red arrow, corresponds to a particular model output. The probability distribution of these outcomes characterise the uncertainty at each time point.

Growth pattern of Gauss-Patterson sparse grid

dimension level	1	2	3	4	5
0	1	1	1	1	1
1	3	5	7	9	11
2	7	17	31	49	71
3	15	49	111	209	351
4	31	129	351	769	1,471
5	63	321	1,023	2,561	5,503
6	127	769	2,815	7,937	18,943
7	255	1,793	7,423	23,297	61,183
8	511	4,097	18,943	65,537	187,903

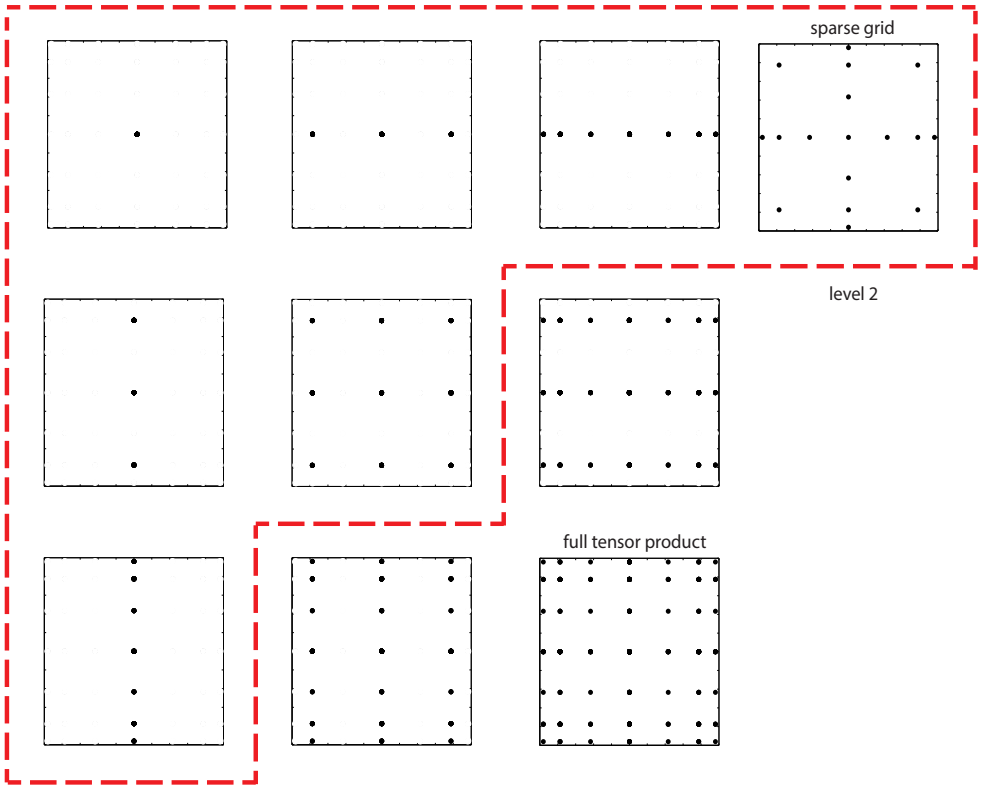

FIGURE 2. Growth pattern of the Gauss-Patterson quadrature rule in dimensions one to five. The numbers in red correspond to the linear combination of the tensor product of the sub-spaces enclosed by the dashed red line collected according to Eq. (18). The resulting sparse grid is shown on the right. Sparse grids can approximate integrals numerically with roughly the same polynomial accuracy as that of the full tensor product (shown on the bottom right), using fewer model evaluations. The difference in the number of nodes reaches orders of magnitude in higher dimensions, e.g., the full tensor product in five dimensions corresponding to level eight would require $511^5 = 34842114263551$ model evaluations.

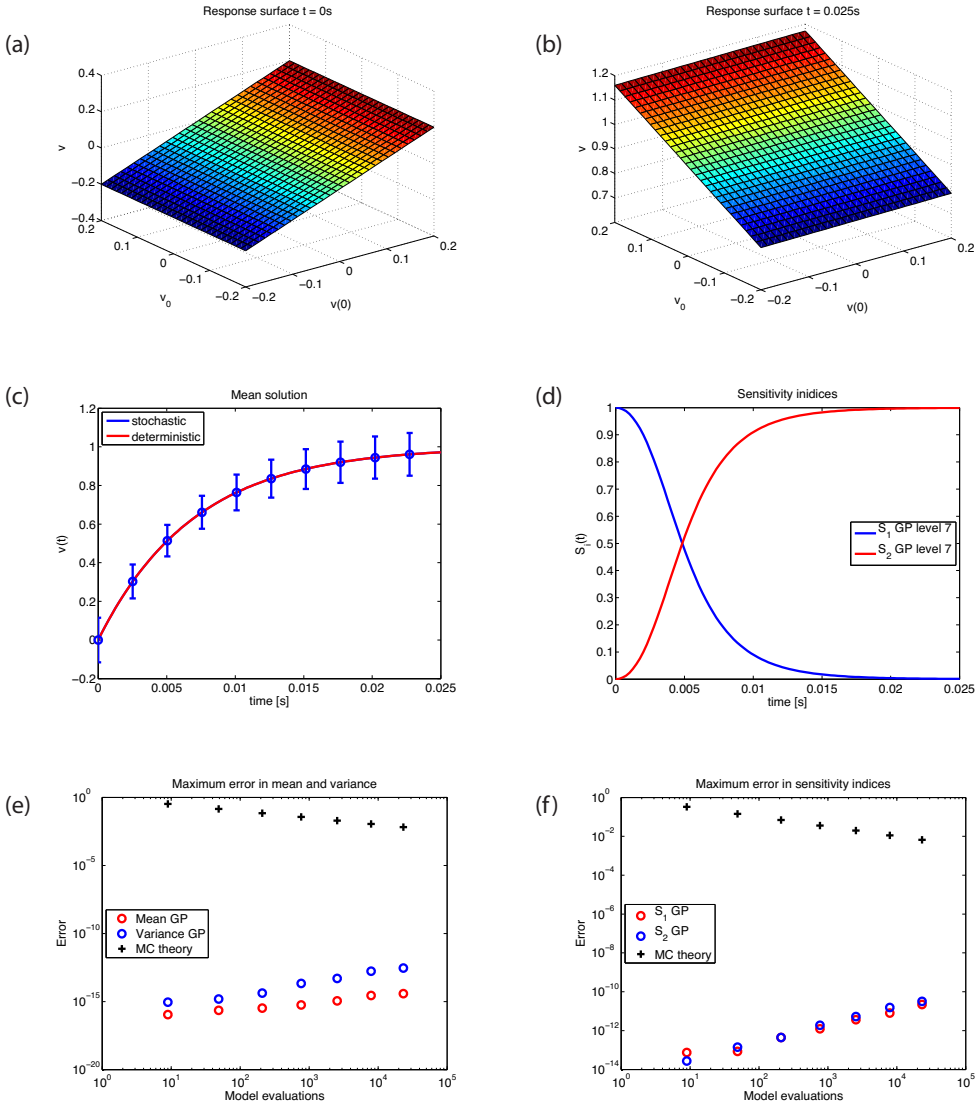

FIGURE 3. Uncertainty analysis for an example of linear dependence in the stochastic parameters (example 1). (a) and (b) show the response surface at different times, which determines how the random parameters affect the model output. As time marches on the slope of the intersection with any plane orthogonal to the $v(0)$ axis vanishes, indicating that the initial condition no longer influences the model's output variability, in agreement with (d), where the corresponding sensitivity indices are presented. (c) shows the model output with error bars extending one standard deviation above and below the mean. In this linear example the mean stochastic and deterministic solution coincide. (e) and (f) show the error for all quadratures required for the analysis as a function of model evaluations (grid points). For such a simple response surface, quadratures can be computed exactly with very few grid points. Increasing the number of model evaluations introduces round-off error. The theoretical convergence rate of the crude Monte Carlo method (one divided by the square root of the number of model evaluations) is shown for comparison.

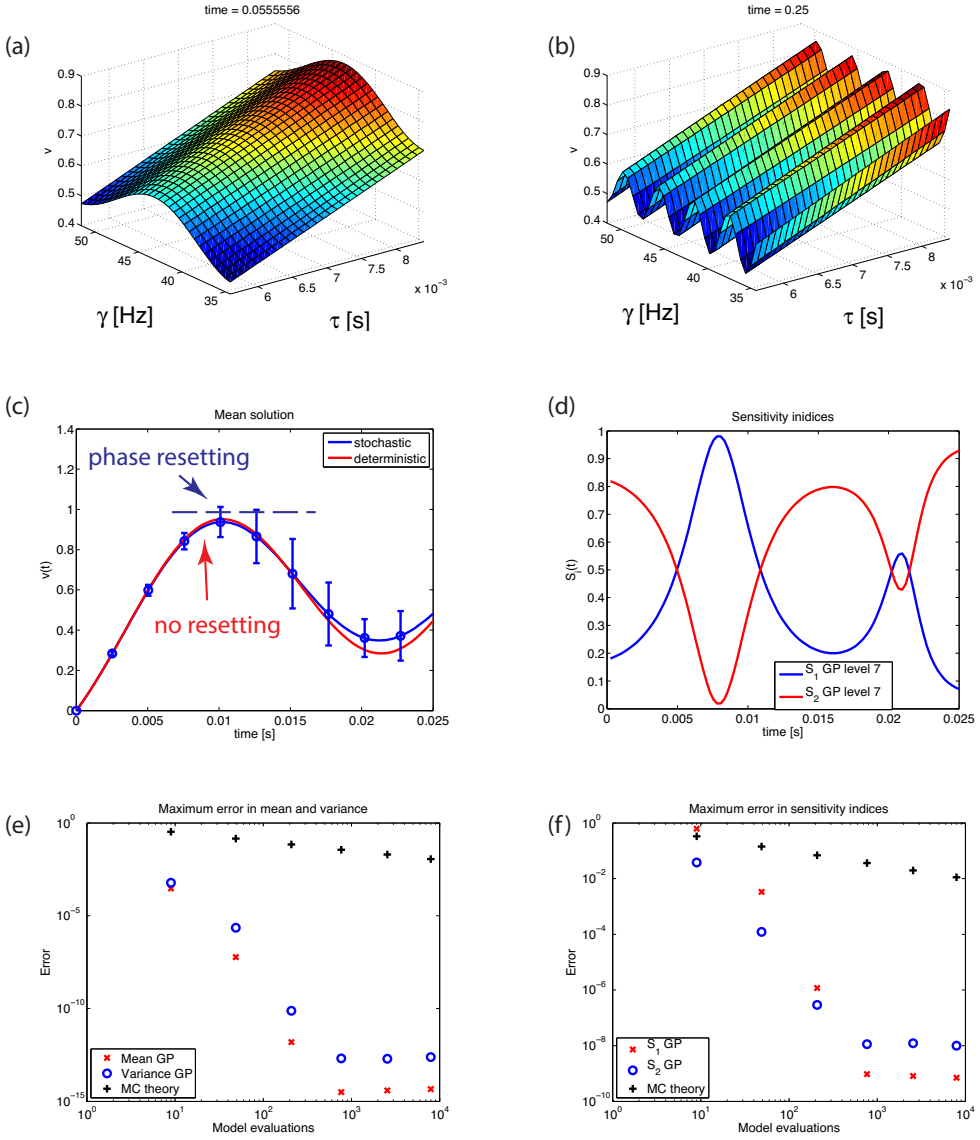

FIGURE 4. Uncertainty analysis for an example of nonlinear dependence in the stochastic parameters (example 2). (a) and (b) show the response surface for different times which, in contrast to that in Fig. 3, is highly nonlinear. (c) shows the model output with error bars extending one standard deviation above and below the mean. Notice that the deterministic solution differs considerably from the mean stochastic solution. (d) shows the corresponding sensitivity analysis, revealing uncertainty in γ as the main source of variability in (c) for the second half of the time series. Errors for all quadratures required for the analysis are shown in (e) and (f), which indicate that in spite of the nonlinearity of the response surface, the integrals required for the uncertainty analysis can be obtained accurately. (c) shows how the deterministic and stochastic models can yield different phase resetting responses, which according to the model, occur when the membrane potential gets larger than one.

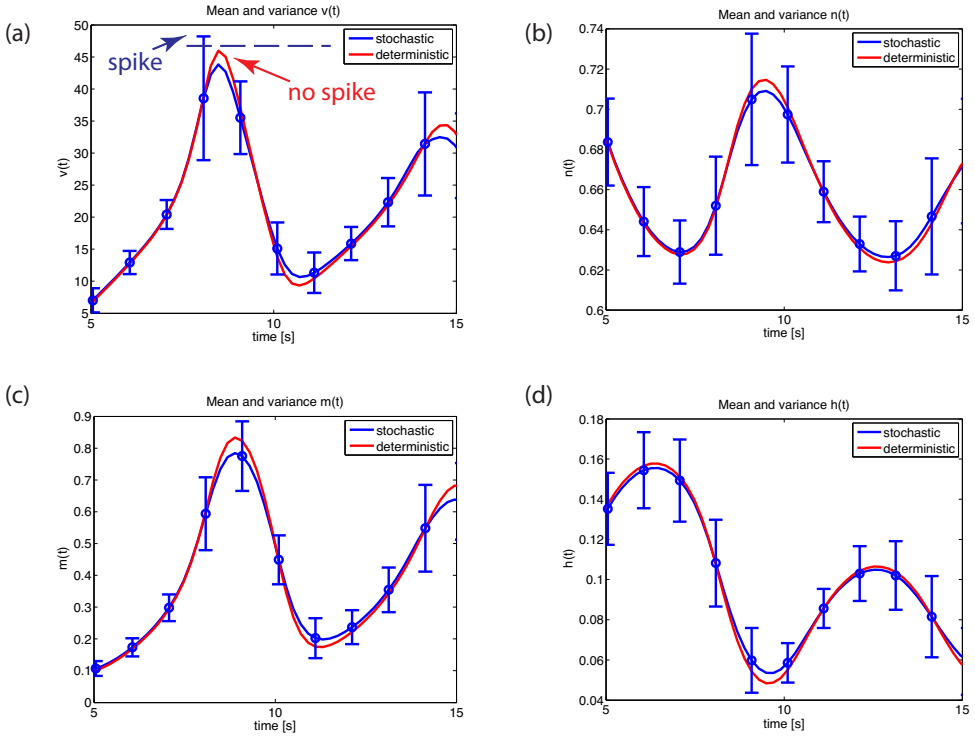

FIGURE 5. Uncertainty propagation in the classical Hodgkin-Huxley model of action potentials. (a) shows the stochastic membrane potential with error bars extending one standard deviation above and below the mean. (b), (c) and (d) show the dynamics of the gating variables. In all cases the deterministic and mean stochastic solutions are shown for comparison. (a) shows how setting a threshold for spike detection can yield different results when uncertainty is incorporated in the model as compared to the deterministic case.

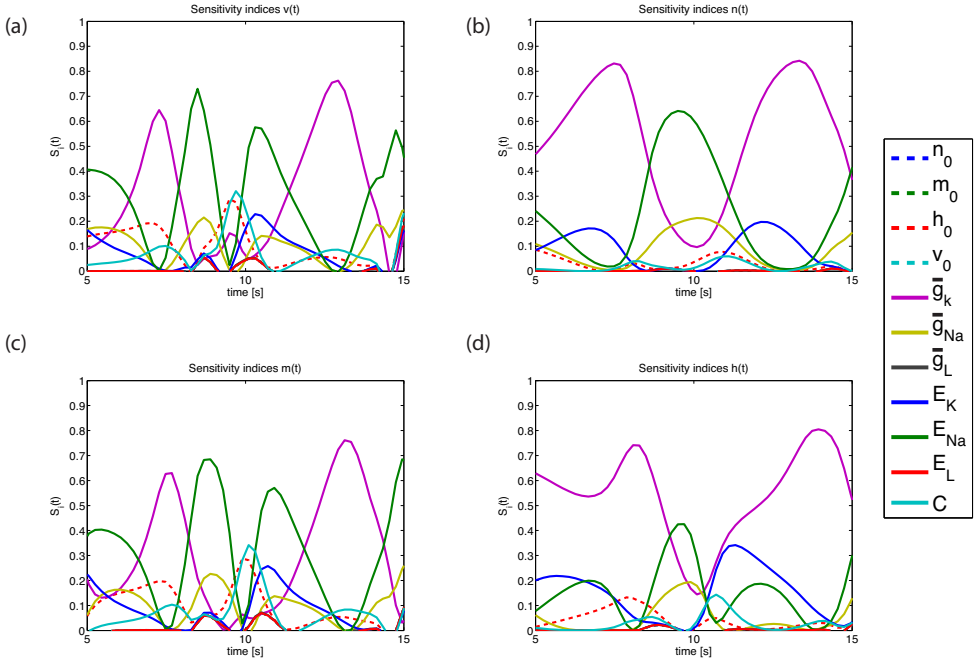

FIGURE 6. Sensitivity analysis of the classical Hodgkin-Huxley model. The panels show sensitivity indices for the membrane potential and the gating variables as indicated in the legends. The sensitivity analysis reveals two main sources of probabilistic uncertainty, namely $\overline{g}_k$ and E_{Na}. The influence of all the other parameters in the variability of the model output is small, so they can be fixed to their nominal values reducing considerably the dimensionality of the problem whilst retaining most of the stochastic features of the model. This can facilitate simulations involving multiple cells, where only two parameters per cell can be used instead of eleven.

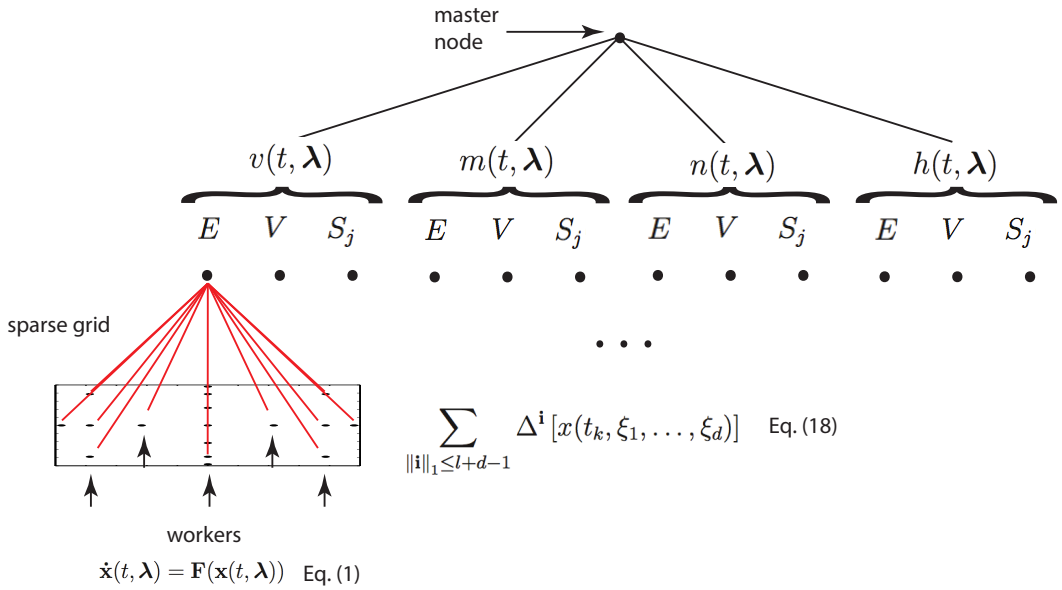

FIGURE 7. An example of algorithm parallelization considering the Hodgkin-Huxley model. All quadratures required for uncertainty analysis can be performed simultaneously, for they employ different data. These data are generated through model evaluations at distinct regions of the probability space as illustrated in the bottom left corner. The model evaluations can be performed by different workers (processes) which do not need to communicate among them. Their contributions to the quadrature are collected in the master node and added to obtain the values of the mean, variance and sensitivity indices for all time points in parallel. Such parallelization can effectively reduce the wall clock time required for the uncertainty analysis and opens the possibility of studying larger scale systems such as neural networks.

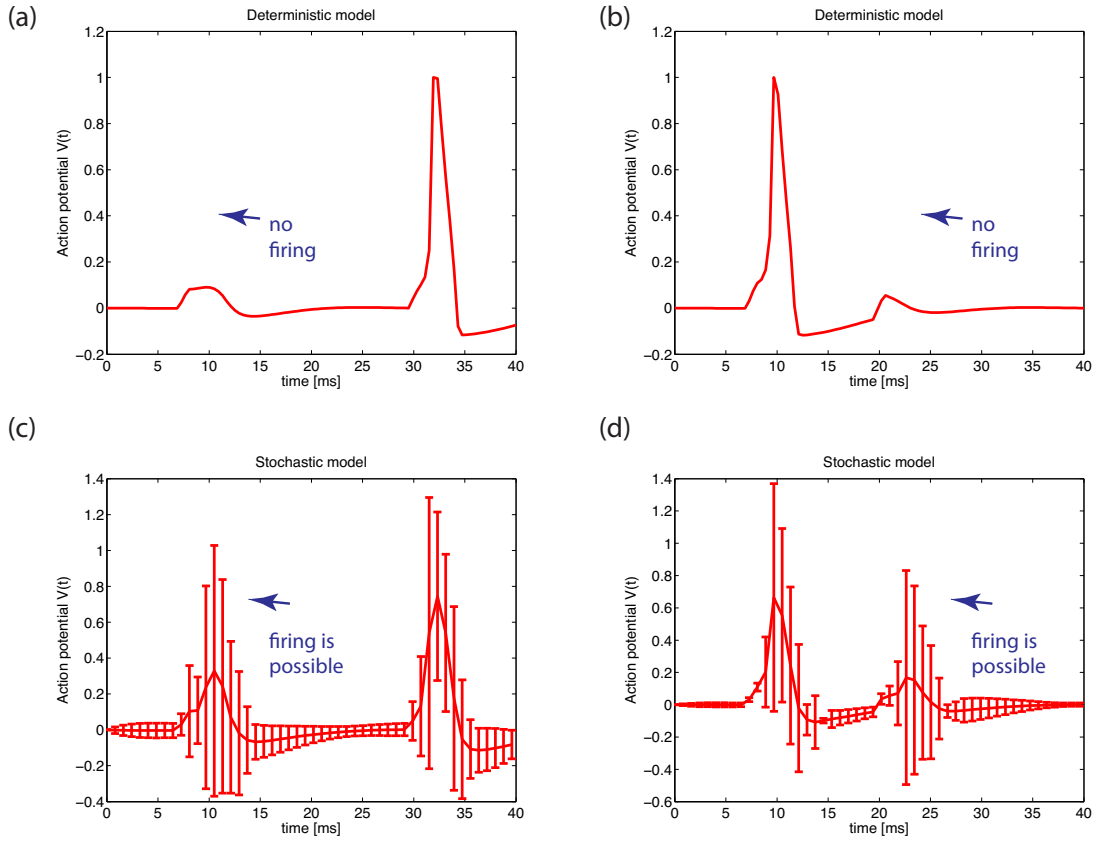

FIGURE 8. Some effects of probabilistic uncertainty in the HH model response to an external current input. The left panels show the response of the deterministic model to two current pulses of different amplitude. The first pulse results in a small perturbation of the membrane potential, which returns to equilibrium shortly after the pulse have been applied. The second pulse produces a perturbation that is greatly amplified generating a spike. On the other hand, under uncertainty conditions, Fig. (c), the small current pulse can cause the neuron to fire. In the panels on the right the large pulse is applied first firing the neuron. In the deterministic case (b), the refractory period prevents the neuron from being fired by the second pulse, in the stochastic model (d), the neuron could fire a second spike.

TABLE 1. RMS error for the model illustrated in Figs. 5 and 6.

	E	σ	S_{n_0}	S_{m_0}	S_{h_0}	v_0	$S_{\overline{g}_k}$	$S_{\overline{g}_{Na}}$	$S_{\overline{g}_L}$	S_{E_K}	$S_{E_{Na}}$	S_{E_L}	S_C
$n(t)$	0.000163	0.000350	0.016969	0.016969	0.016710	0.016970	0.012563	0.009419	0.016891	0.015160	0.011181	0.016949	0.015736
$m(t)$	0.001494	0.004814	0.090669	0.090668	0.089543	0.090673	0.097756	0.057230	0.090059	0.078554	0.062516	0.090535	0.082084
$h(t)$	0.000112	0.000271	0.046205	0.046205	0.045488	0.046202	0.035574	0.027616	0.045989	0.042473	0.017223	0.046155	0.042037
$v(t)$	0.004669	0.052106	0.087004	0.087002	0.084896	0.086993	0.079195	0.055766	0.086538	0.073698	0.060872	0.086917	0.078468

TABLE 2. RMS error for the model illustrated in Fig. 8(a).

	E	σ	g_k	E_{Na}
$n(t)$	0.001564	0.000880	0.083202	0.089970
$m(t)$	0.003198	0.005161	0.082879	0.089434
$h(t)$	0.001229	0.001007	0.064681	0.099141
$v(t)$	0.002727	0.004468	0.118777	0.061285

TABLE 3. RMS error for the model illustrated in Fig. 8(b).

	E	σ	$\overline{g}_k$	E_{Na}
$n(t)$	0.005049	0.001422	0.368499	0.205062
$m(t)$	0.007794	0.006030	0.479935	0.225715
$h(t)$	0.005618	0.001785	0.293118	0.228673
$v(t)$	0.005881	0.004275	0.420290	0.206227